NOTE

Magnetic Resonance in Medicine 00:00–00 (2014)

Sliding Time of Flight: Sliding Time of Flight MR Angiography Using a Dynamic Image Reconstruction Method

Joonsung Choi,[1] Hyunseok Seo,[1] Yongwan Lim,[1] Yeji Han,[1,2] and HyunWook Park[1]*

Purpose: To obtain three-dimensional (3D) MR angiography having high contrast between vessel and stationary background tissue, a novel technique called sliding time of flight (TOF) is proposed.

Methods: The proposed method relies on the property that flow-related enhancement (FRE) is maximized at the blood-entering slice in an imaging slab. For the proposed sliding TOF, a sliding stack-of-stars sampling and a dynamic MR image reconstruction algorithm were developed. To verify the performance of the proposed method, in vivo study was performed and the results were compared with multiple overlapping thin 3D slab acquisition (MOTSA) and sliding interleaved k_y (SLINKY).

Results: In MOTSA and SLINKY, the variation of FRE resulted in severe venetian blind (MOTSA) or ghost (SLINKY) artifacts, while the vessel-contrast increased as the flip angle of radiofrequency (RF) pulses increased. On the other hand, the proposed method could provide high-contrast angiograms with reduced FRE-related artifacts.

Conclusion: The sliding TOF can provide 3D angiography without image artifacts even if high flip angle RF pulses with thick slab excitation are used. Although remains of subsampling artifacts can be present in the reconstructed images, they can be reduced by MIP operation and resolved further by regularization techniques. **Magn Reson Med 000:000–000, 2014. © 2014 Wiley Periodicals, Inc.**

Key words: MOTSA; stack-of-stars trajectory; sliding slab; TOF

INTRODUCTION

Time of flight (TOF) is one of the most frequently used MR angiography methods (1,2), which enhances the contrast between vessels and stationary tissues by inducing a flow-related enhancement (FRE) effect. Generally, two-dimensional (2D) TOF covers the target imaging volume by acquiring a set of thin slices, ensuring that the inflowing blood experiences only a limited number of radiofrequency (RF) pulses and that the blood-tissue contrast is enhanced by an RF pulse with a high flip angle. Alternatively, 3D TOF can be used for higher signal-to-noise ratio (SNR) and higher slice resolution but it cannot provide as high contrast as 2D TOF because the FRE is diminished as the in-flowing blood is repeatedly influenced by multiple RF pulses while it traverses through the thick 3D slab. Therefore, RF pulses with a low flip angle are commonly used in 3D TOF (3).

Many 3D-TOF studies have focused on ways to obtain sufficient image quality, which include the multiple overlapping thin slab acquisition (MOTSA) technique (4–6), the use of tilted optimized nonsaturating excitation (TONE) pulses (7), and sliding interleaved k_y (SLINKY) (8,9). Although the MOTSA technique alleviates the inadequate contrast issue to a certain extent, the slab thickness is limited by the velocity of the blood-flow and the venetian blind artifact between adjacent slabs is introduced (3). The venetian blind artifact can be greatly removed by the sliding sampling scheme used in SLINKY, but the ghost artifacts caused by the flow-related signal decay and the interleaved k-space sampling are additionally induced (8). While a more recent algorithm had successfully reduced the ghost artifacts by combining SLINKY with cylinder trajectory, the use of averaged vessel intensities from the blood-entering and the blood-exiting slices may result in a reduced contrast in the angiogram (9).

In this study, a novel technique called sliding TOF to achieve high vessel-to-background contrast angiography and reduced venetian blind artifact is proposed by uniquely combining the sliding stack-of-stars sampling scheme and a dynamic reconstruction algorithm. The proposed method can be characterized by the following features: (a) High vessel-to-background contrast angiography is guaranteed without additional image artifacts; (b) FRE is equalized across the whole imaging volume; and (c) No venetian blind artifact is present. Experimental results are provided in the following sections to validate the performance of the proposed method using in vivo imaging.

METHODS

Saturation of Blood Flow in TOF Angiography

In TOF angiography with a spoiled gradient-echo sequence, the signal (S_j) can be modeled based on several imaging parameters as:

[1]Department of Electrical Engineering, Korean Advanced Institute of Science and Technology (KAIST), Daejeon, South Korea.

[2]Department of Biomedical Engineering, College of Health Science, Gachon University, Incheon, South Korea.

Grant sponsor: The National Research Foundation of Korea (NRF) grant funded by the Korean government (MEST); Grant number: 2012-0000125; Grant sponsor: Basic Science Research Program through the National Research Foundation of Korea (NRF) funded by the Ministry of Science, ICT & Future Planning; Grant number: 2013R1A1A3009909.

*Correspondence to: HyunWook Park, Ph.D., Department of Electrical Engineering, KAIST, 335 Gwahangno, Yuseong-gu, Daejeon 305-701, South Korea. E-mail: hwpark@kaist.ac.kr

Received 6 January 2014; revised 8 February 2014; accepted 19 February 2014

DOI 10.1002/mrm.25215

Published online 00 Month 2014 in Wiley Online Library (wileyonlinelibrary.com).

© 2014 Wiley Periodicals, Inc.

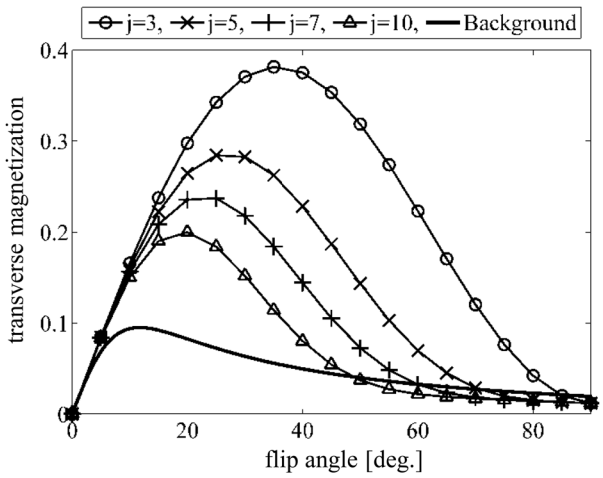

FIG. 1. Plots of normalized intensities of the transverse magnetization (M_{xy}) of blood (for $j = 3$, $j = 5$, $j = 7$, and $j = 10$) and white matter (*background*) with respect to flip angles and number of RF pulses applied to tissue. Vertical axis has an arbitrary unit when the unsaturated M_{xy} has the value of 1. Background means equilibrium signal intensities from the series of RF pulses.

$$S_j = M_0 \sin\theta[f_{z,SS} + (\cos\theta \cdot e^{-\mathrm{TR}/\mathrm{T}_1})^{j-1}(1 - f_{z,SS})]e^{-\mathrm{TE}/\mathrm{T}_2^*},$$
$$\text{for } f_{z,SS} = \frac{1 - e^{-\mathrm{TR}/\mathrm{T}_1}}{1 - \cos\theta \cdot e^{-\mathrm{TR}/\mathrm{T}_1}} \quad [1]$$

where M_0 denotes the longitudinal magnetization at equilibrium state, T_2^* is relaxation time caused by a combination of spin-spin relaxation and magnetic field inhomogeneity, j is the number of experienced RF pulses, and θ is the flip angle of the RF pulse (3). Based on Eq. [1], the normalized signal intensity of partially saturated magnetization can be plotted with respect to the flip angle θ, as presented in Figure 1. To demonstrate signal characteristics, T_1 of 1900 ms and T_2 of 300 ms for blood were assumed for blood, and T_1 of 1100 ms and T_2 of 70 ms were assumed for white matter (representing stationary background tissue) (10). Repetition time (TR) and echo time (TE) were set as 23 ms and 5 ms, respectively. In Figure 1, the vertical axis represents the signal intensities of the transverse magnetization (M_{xy}) of blood (for $j = 3$, $j = 5$, $j = 7$, and $j = 10$) and white matter (*background*), where the equilibrium magnetization M_0 has the value of 1. As suggested by Figure 1, the intensity of the signal increases as the total number of applied excitation pulses decreases and a high flip angle of 50–70° can be used in the conventional 2D TOF because the arterial flow, with a typical velocity of 10–100 cm/s, normally experiences only one or two RF pulses ($j = 1 \sim 2$) (3). On the other hand, low flip angle is preferred in the 3D TOF to prevent rapid signal saturation when large numbers of RF pulses are applied.

Data Acquisition and Reconstruction

The proposed method uses the property that the FRE is always maximized at the blood-entering slice in an imaging slab. In this study, a total imaging volume was composed of multiple 3D slabs, where the sliding distance between adjacent slabs was set to the slice thickness. By covering the total imaging volume with sliding slabs, the maximum FRE information of every slice can be extracted when the specific slice acts as a blood-entering slice for a specific 3D slab. However, the sliding-slab concept requires redundant sampling and increased acquisition time. Therefore, a highly subsampled radial trajectory, which can be efficiently combined with dynamic image reconstruction, is used for the proposed sliding TOF. More specifically, data is acquired using a 3D hybrid radial (called the stack-of-stars) trajectory, as schematically described in Figure 2, where (k_r, ϕ) denotes the radial k-space, k_z is the z-direction of the k-space, and s is a slab index. For the k_z direction, the sampling rate is determined by the Nyquist rate to avoid aliasing artifacts along the slice direction. However, abiding by the Nyquist condition is less important in the (k_r, ϕ) domain and the number of projection views can be considerably reduced. For the acquisition order of the projection data in the proposed method, the golden angle ratio technique was adopted because it keeps the incremental angle of the successively acquired projection data constant; even for an arbitrary number of projection views (11). Based on the golden angle ratio, the angle for each projection view is determined as follows:

$$\phi_{n_v,s} = \mathrm{mod}(111.25 \times (n_v + s \times N_v), 360),$$
$$\text{for } n_v = 0, 1, \ldots, N_v - 1, \;\; s = 0, 1, \ldots, S, \quad [2]$$

where $\phi_{n_v,s}$ denotes the angle of the n_v-th projection view at the s-th slab, N_v is the number of views for a single slab, and mod(x,y) means x modulus y.

Image Reconstruction

After acquiring the 3D data, 1D Fourier transform is performed along the z direction of each 3D slab to extract 2D radial k-space data at $z = z'$ as shown in Figure 2a. When data are acquired with a sliding scheme, the intensities influenced by the FRE would be different according to their relative z-directional positions in each slab as represented in Figure 2b; the projection data of the slice near the blood-entering boundary of each slab shows high FRE, and the FRE decreases as the distance from the blood-entering slab boundary increases. In other words, when the whole projection data set from the same anatomical slices are used to generate a composite image, the vessel intensities are averaged and the contrast will be reduced as shown in Figure 1b. Thus, the limited number of projection data with high FRE is used in the proposed method as a "seed-sinogram" to preserve the high-contrast vessel-to-background information. More specifically, the complex expectation maximization (EM) algorithm (12,13) is used while treating the vessel intensity, which changes according to the number of experienced RF pulses, as dynamic information. In the complex EM algorithm, the reconstructed image, I_{recon}, is iteratively reconstructed by using boundary information, B^L and B^U, that satisfy $real(B^L) \leq real(I_{recon}) \leq real(B^U)$ and $imag(B^L) \leq imag(I_{recon}) \leq imag(B^U)$. where $real(x)$ and $imag(x)$ are the operators to extract real and

imaginary values of x, respectively. The iterative process can be described as follows:

$$C_{k+1} = \frac{I_k^L \times B^U + I_k^U \times B^L}{I_k^L + I_k^U}.$$

$$I_k^L = real\,(C_k^L) \cdot \frac{real(\boldsymbol{R}^{-1}S^L)}{real(\boldsymbol{R}^{-1}(\boldsymbol{R}C_k^L))} + i \times imag(C_k^L) \cdot \frac{imag(\boldsymbol{R}^{-1}S^L)}{imag(\boldsymbol{R}^{-1}(\boldsymbol{R}C_k^L))},$$

$$I_k^U = real\,(C_k^U) \cdot \frac{real(\boldsymbol{R}^{-1}S^U)}{real(\boldsymbol{R}^{-1}(\boldsymbol{R}C_k^U))} + i \times imag(C_k^U) \cdot \frac{imag(\boldsymbol{R}^{-1}S^U)}{imag(\boldsymbol{R}^{-1}(\boldsymbol{R}C_k^U))}. \quad [3]$$

where $S^L = S - \boldsymbol{R}B^L,\ S^U = \boldsymbol{R}B^U - S$ and

$$C_k^L = C_k - B^L,\ C_k^U = B^U - C_k.$$

In Eq. [3], $\boldsymbol{R}$ and $\boldsymbol{R}^{-1}$ denote the Radon transform and its inverse transform, respectively, and C_k is the k-th iterated result. The composite image is used as the initial image (C_0) and S is the seed-sinogram. The actual number of projection views required for a proper seed-sinogram is dependent upon the velocity and the direction of the blood flow. If the velocity of the blood flow is high, more projection data from nearby slices can be used to generate a seed-sinogram because the saturation effect is not severe. After a total of K iterations, the K-th result image, C_K, becomes the flow-enhanced image I_{recon}.

In the proposed method, the extracted seed-sinograms for vessels flowing in opposite directions ($+z$, $-z$) can be independently used to explicitly emphasize the vessels flowing in the +z or −z directions. Alternatively, both images with flows enhanced in the opposite directions can be reconstructed and the maximum intensity value from two result images can be chosen on a voxel by voxel basis to generate a final FRE maximized angiography image that is independent of flow direction.

In Vivo Experiments

In vivo experiments were performed to validate the overall performance of the proposed method by acquiring cerebral angiography images at a 3 Tesla (T) MRI scanner (Siemens Magnetom Verio, Erlangen, Germany). All experimental sessions were approved by the KAIST Institutional Review Board and written informed consent forms were signed by all participants.

The first experiment was performed on 10 healthy volunteers (age: 26.5 ± 2.5 years) with a venous saturation RF pulse (flip angle = 90°, thickness = 40 mm, and the gap between the saturation and imaging regions is 10 mm) to compare the proposed method with the Cartesian MOTSA and SLINKY, and the second experiment was performed on one healthy volunteer (age: 28 years) without the venous saturation RF pulse to analyze the properties of two images reconstructed for the opposite directional flows in the proposed method. For the first experiment, data were acquired with the proposed method, MOTSA with TONE RF pulses, and SLINKY using the following parameters: TR/TE = 23 ms/5 ms, field of view (FOV) of a single slab = 230 × 230 × 20 mm^3, number of sampling points (N_p) = 256, number of phase encodings (N_{pe}) = 256 (MOTSA and SLINKY), number of views (N_v) = 20 (proposed method), number of slices per slab (N_s) = 20, number of slabs (N_{slab}) = 5 (MOTSA)/80 (SLINKY and the proposed method), voxel size = 0.9 × 0.9 × 1 mm^3, total longitudinal FOV = 80 mm, and flip angle = 18° and 36°. For the proposed method, the projection data of a slice were gathered from four successive slabs to compose a seed-sinogram and only the vessels flowing in the upward ($+z$) direction were enhanced for comparison. For MOTSA, four slices per slab were overlapped. To quantitatively analyze the results, the contrast-to-noise ratio (CNR) was calculated as

$$CNR = \frac{S_{vessel} - S_{background}}{\sigma} \quad [4]$$

where S_{vessel} and $S_{background}$ are the signal intensities of the vessel and the background tissue, respectively, and σ is the standard deviation of the image noise. For the second experiment, the imaging parameters were set as follows: TR/TE = 22 ms/5.45 ms, FOV of a single slab = 280 × 280 × 20 mm^3, total longitudinal FOV = 80 mm, $N_p \times N_v \times N_s \times N_{slab}$ = 384 × 30 × 20 × 80, shift amount = 1 mm, and flip angle = 60°. The projection data from two successive slices were used to compose seed-sinograms for each ($+z$ or $-z$) directional flows and final images were reconstructed to provide an image resolution of 0.7 × 0.7 × 1 mm^3. All reconstruction algorithms were implemented using MATLAB (The Mathworks, Inc., Matrick, MA). In MATLAB implementation, reconstruction of each image using 30 iterations requires 20 s. Therefore, a total of 106 min was required to reconstruct 240 images (80 slices × 4 channels) having an in-plane matrix size of 256 × 256.

RESULTS

Figure 3 shows the axial and coronal MIP images from the MOTSA, SLINKY, and the proposed methods (Figs. 3a–c,e–g). While none of the results show image artifacts in Figures 3a–c, the vessel-to-background contrasts were also low due to the low flip angle. A high flip angle (36°) could be used to increase the vessel contrast (Figure 3e–g). However, the rapidly decreased FRE caused the venetian blind artifacts in MOTSA (Fig. 3e) and the change in the vessel signal intensities across the imaging slabs caused the ghost artifacts in SLINKY (Fig. 3f). Meanwhile, the proposed method generated high vessel-to-background contrast without venetian blind artifact or ghost artifact (Fig. 3h). Figures 3d and 3h show MIP images reconstructed from retrospectively subsampled projection data, thereby satisfying a condition of similar imaging time where the acquisition times of the proposed method and MOTSA/SLINKY are similar (the number of projection views for composite image = 260 (13 views per slice × 20 slices) and N_{pe} = 256). For the subsampled data set, the seed-sinogram was composed

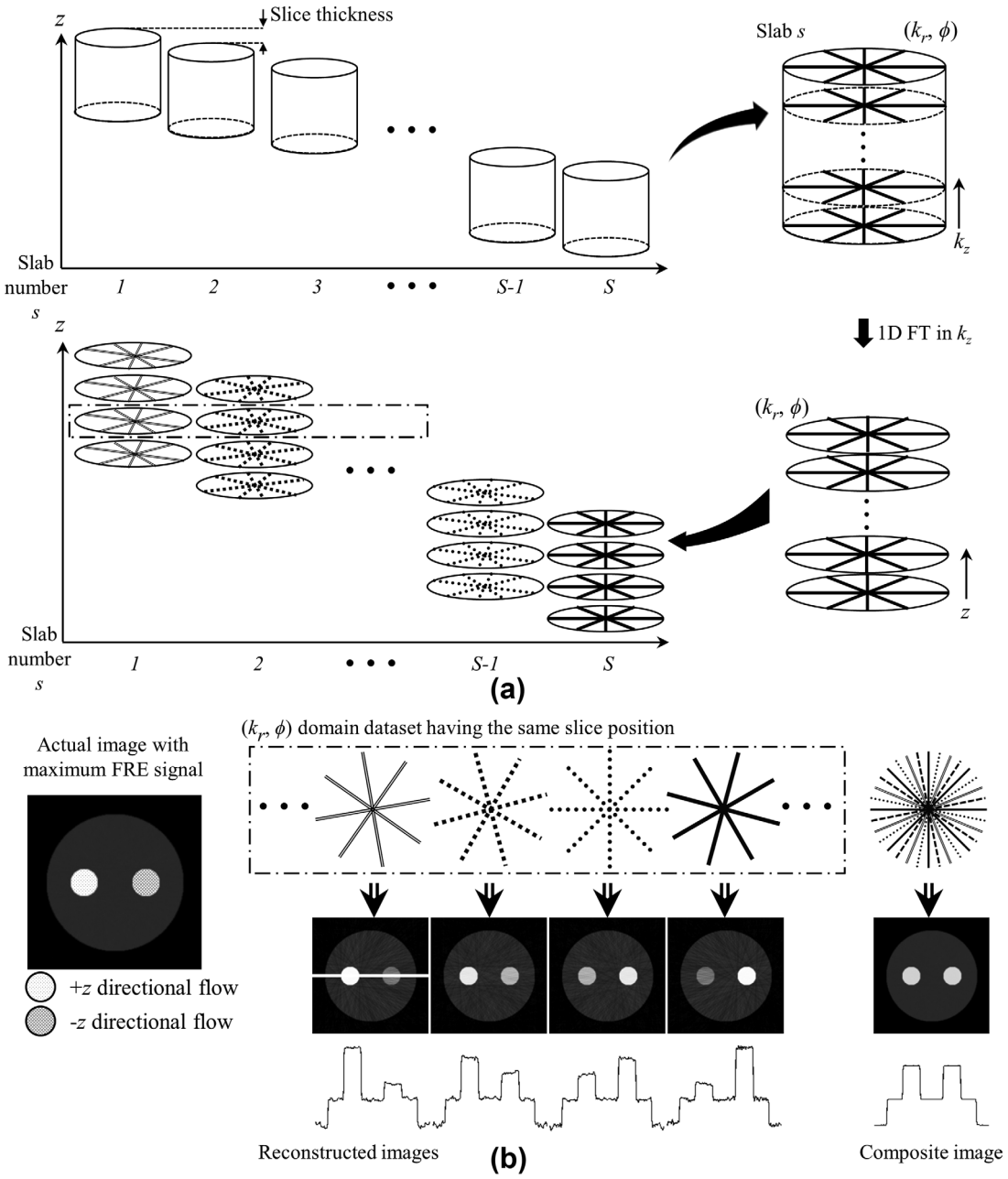

FIG. 2. Data acquisition scheme of sliding TOF. **a:** The 3D slab is acquired at slab index *s* using a stack-of-stars trajectory with reduced projection views and the slab is sliding by a one-slice shift to cover the whole imaging volume. Then, the slab data are Fourier-transformed in the *z*-direction and converted to (k_r, ϕ, z, s) domain. **b:** These sinograms at certain slice positions are processed to reconstruct images with different FRE and streaking artifacts. The image intensities of vessels vary according to the flow direction and the number of applied RF pulses. On the other hand, the composite image obtained from all the projection data has much reduced streaking artifacts and averaged vessel intensities.

of four successive slices. Although the subsampled projection data that did not satisfy the Nyquist rate caused streaking artifacts, the MIP images were acceptable as the artifacts were not shown in the MIP images because they were typically in the range of the background tissue signal.

In addition, the CNR between the internal carotid artery (ICA) and the stationary tissue was obtained at the blood-entering and the blood-exiting slices on the ROIs defined as shown in Figure 4a. As plotted in Figure 4b, MOTSA, SLINKY, and the proposed method with the number of projection views for composite image = 260 showed similar CNR for flip angle = 18°, and the CNR in the proposed method with the number of projection views for composite image = 400 was slightly high. For flip angle = 36°, the CNR at the blood-exiting slice from MOTSA decreased significantly due to the rapid signal saturation. Although the CNR did not decrease at the blood-exiting slice from SLINKY due to the sliding sampling scheme, the CNR values were relatively low due to

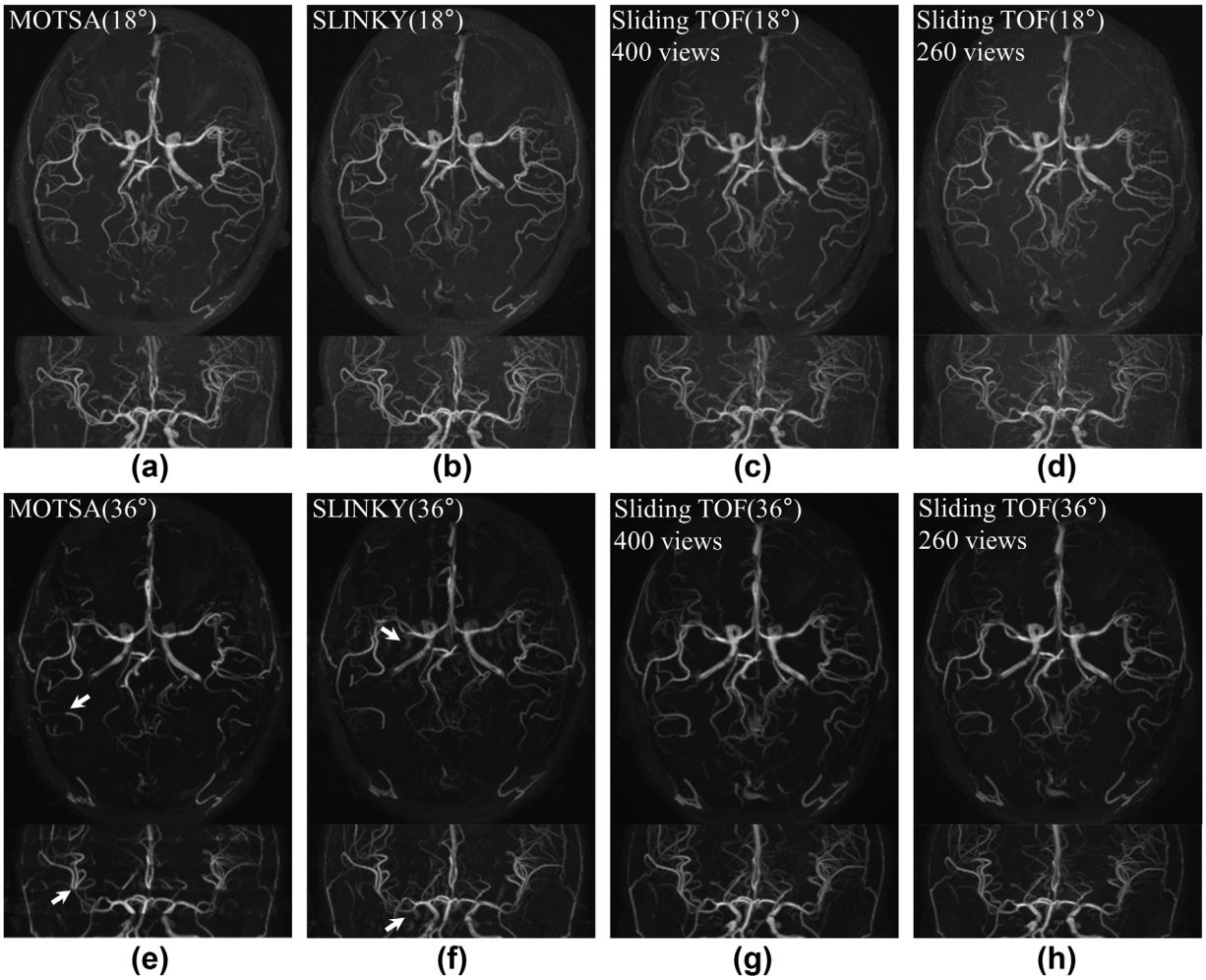

FIG. 3. In vivo results from MOTSA, SLINKY and the proposed methods. The images show the MIP results of axial and coronal directions. MIP images with flip angle of 18° from MOTSA (**a**), SLINKY (**b**), the sliding TOF (400 views) (**c**), and the sliding TOF (260 views) (**d**). The results of high flip angle of 36° are shown in bottom row images with MOTSA (**e**), SLINKY (**f**), the sliding TOF (400 views) (**g**), and the sliding TOF (260 views) (**h**).

the signal loss caused by ghost artifacts. On the other hand, the CNR from the sliding TOF were generally high even at the blood-exiting slice.

To demonstrate the properties of the two opposite directional angiograms, the sagittal and coronal directional MIP images were reconstructed from the data set acquired from the second experiment. The upper and middle row images of Figure 5 show the MIP results of the angiograms generated for the upward ($+z$) and the downward ($-z$) vessel flows, respectively. The artery and the vein mainly appeared in Figures 5a and 5b, respectively, because the arterial blood flows in the $+z$ direction and the venous blood flows in the $-z$ direction in most cases. By taking the maximum value of the two angiograms, the artery and vein can be mutually visualized as shown in Figure 5c.

DISCUSSION

In conventional 2D and 3D TOF angiography, there is a tradeoff between vessel-to-background contrast and slice resolution (or SNR). Thus, advanced techniques such as MOTSA and SLINKY have improved this issue in various ways. However, the flip angle has to be carefully determined by considering the tradeoff between the venetian blind artifact and the vessel-to-background contrast in MOTSA. The sliding sampling scheme used in SLINKY enabled the use of higher flip angles but the changes of vessel signals due to flow signal saturation resulted in the ghost artifacts. More recently, the cylindrical trajectory was combined with SLINKY (9) to prevent the ghost artifacts but it failed to provide high vessel-to-background contrast because the image was reconstructed by averaging the data acquired at different slabs. Therefore, the proposed sliding TOF adopted the sliding scheme of SLINKY for the use of a high flip angle and the stack-of-stars trajectory to remove the ghost artifacts. In addition, the dynamic image reconstruction algorithm was used to reconstruct images from the limited number of projection data. As demonstrated by the experiments, deficiency in the number of projection data could result in streaking artifacts in the proposed sliding stack-of-stars trajectory but such streaking artifacts can be efficiently removed in MIP results, thereby providing

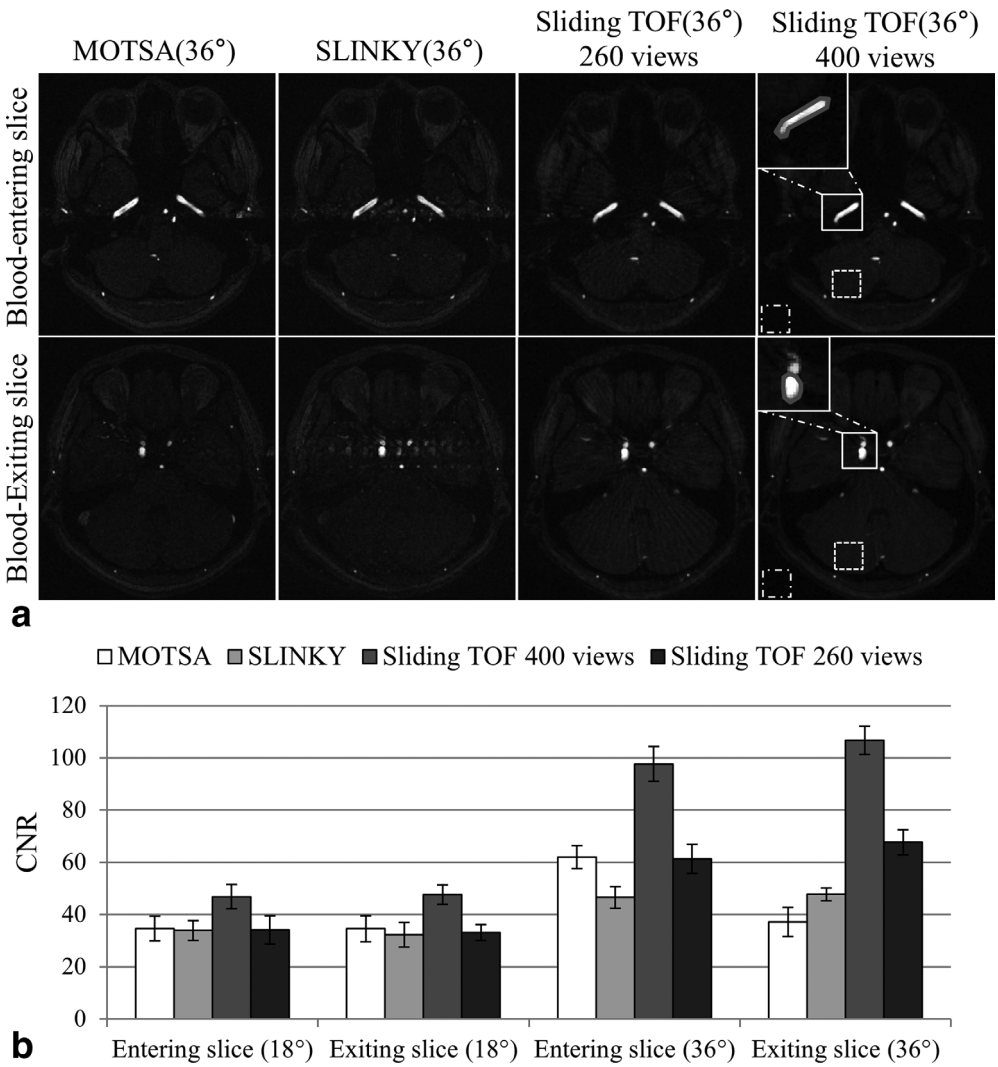

FIG. 4. **a:** The images from MOTSA, SLINKY, the sliding TOF (260 views), and the sliding TOF (400 views) at blood-entering slice position and blood-exiting slice position (flip angle of 36°). For the CNR calculation, ICA (marked with gray line), the background tissue (marked with dotted square), and the noise region (marked with dot-dashed square) are extracted. **b**: The mean and the standard deviation of CNR between ICA and background tissue with different flip angles (18° and 36°) and different slice positions (blood-entering and blood-exiting slices).

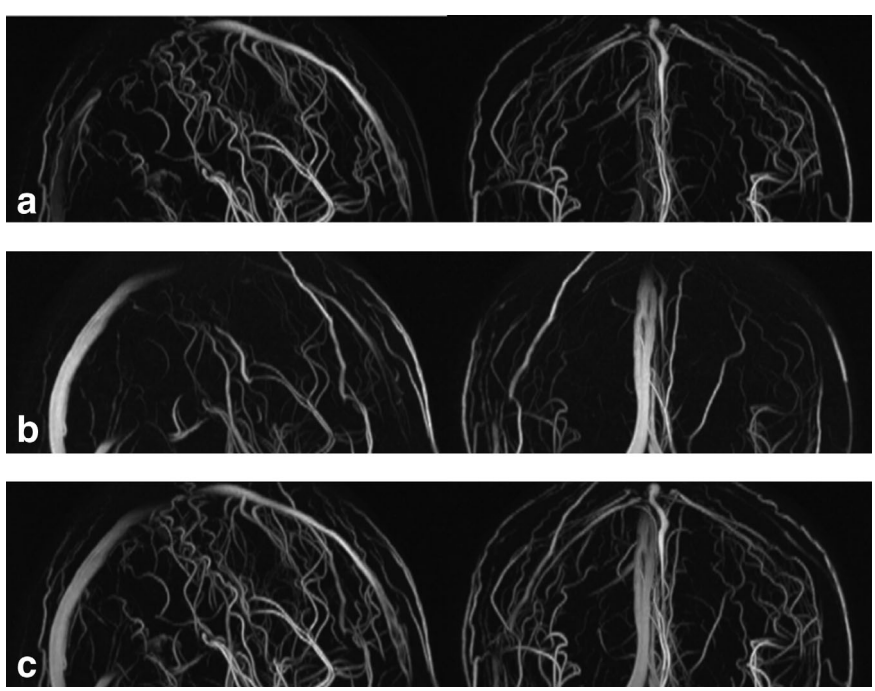

FIG. 5. The MIP results from different seed-sinograms. The sagittal and coronal directional MIP from upward directional (+*z*) seed-sinogram (**a**) and downward directional (−*z*) seed-sinogram (**b**), respectively. By taking the maximum value between two angiograms, final flow-enhanced MIP results can be acquired as shown in (**c**).

artifact-reduced angiogram. In addition, the proposed method can emphasize the vessel signals flowing in $+z$ or $-z$ directions by selectively weighting the signal from the blood-entering slices. However, the signal from vessels that are horizontally oriented in the image slice can be saturated. This characteristic is similar to the other conventional angiography methods.

The proposed method has several limitations that need to be discussed. To satisfy the Nyquist rate, the proposed method requires a longer acquisition time than the Cartesian sampling because the proposed method uses the radial sampling. However, as shown in the MIP images in Figure 3, the proposed method with subsampled data set can still provide a fine performance, meaning that the acquisition time can be reduced by 35% (400 views to 260 views) without degradation of the MIP images. In addition, advanced regularization techniques or parallel imaging techniques are more readily used in radial MRI (14–17), and can be used to further reduce the number of projection views needed. Reduction of the imaging time can be also beneficial for minimization of motion-related errors, which may be achieved more easily in the proposed method and SLINKY than MOTSA because the k-space data acquired at different slabs are combined for image reconstruction. The algorithms that use the sliding concept may be also sensitive to off-resonance artifacts. Therefore, further research should be performed to alleviate such artifacts by using advanced imaging techniques, such as the moving table technique (18,19).

In conclusion, a novel sliding TOF angiography method, comprised of the sliding stack-of-stars sampling scheme and the complex EM reconstruction algorithm, was proposed. The sliding TOF provides high vessel-to-background contrast with high flip angles without any side effects such as venetian blind artifacts and ghost artifacts.

REFERENCES

1. Suryan G. A time-of-flight method. Proc Indian Acad Sci Sect 1959; A33:107.
2. Hinshaw WS, Bottomley PA, Holland GN. Radiographic thin section image of the human wrist by nuclear magnetic resonance. Nature 1977;270:272–273.
3. Bernstein MA, King KF, Zhou XJ. Handbook of MRI pulse sequences. Waltham, MA: Elsevier/Academic Press; 2004.
4. Parker DL, Yuan C, Blatter DD. MR angiography by multiple thin slab 3D acquisition. Magn Reson Med 1991;17:434–451.
5. Blatter DD, Parker DL, Robison RO. Cerebral MR angiography with multiple overlapping thin slab 3D acquisition: I. Quantitative analysis of vessel visibility. Radiology 1991;179:805–811.
6. Blatter DD, Parker DL, Ahn SS, Bahr AL, Robison RO, Schwartz RB, Jolesz FA, Boyer RS. Cerebral MR angiography with multiple overlapping thin slab acquisition. Part II. Early clinical experience. Radiology 1992;183:379–389.
7. Atkinson D, Brant-Zawadzki M, Gillan G, Purdy D, Laub G. Improved MR angiography: magnetization transfer suppression with variable flip angle excitation and increased resolution. Radiology 1994;190: 890–894.
8. Liu K, Rutt BK. Sliding Interleaved ky, (SLINKY) Acquisition: A Novel 3D MRA Technique with Suppressed Slab Boundary Artifact. J Magn Reson Imaging 1998;8:905–911.
9. Kwon KT, Hu BS, Nishimura DG. Peripheral MR venography using sliding interleaved cylinder (SLINCY) imaging. In Proceedings of the 21st Annual Meeting of ISMRM, Salt Lake City, Utah, USA, 2013. Abstract 1282.
10. Stanisz GJ, Odrobina EE, Pun J, Escaravage M, Graham SJ, Bronskill MJ, Henkelman RM. T1, T2 relaxation and magnetization transfer in tissue at 3T. Magn Reson Med 2005;54:507–512.
11. Winkelmann S, Schaeffter T, Koehler T, Eggers H, Doessel O. An optimal radial profile order based on the Golden Ratio for time-resolved MRI. IEEE Trans Med Imaging 2007;26:68–76.
12. Choi J, Kim D, Oh C, Han Y, Park HW. An iterative reconstruction method of complex images using expectation maximization for radial parallel MRI. Phys Med Biol 2013;58:2969–2988.
13. Choi J, Han Y, Park HW, Phase contrast (PC) MR image reconstruction using complex expectation maximization (EM), In Proceedings of the 21st Annual Meeting of ISMRM, Salt Lake City, Utah, USA, 2013. Abstract 2963.
14. Block KT, Uecker M, Frahm J. Undersampled radial MRI with multiple coils. Iterative image reconstruction using a total variation constraint. Magn Reson Med 2007;57:1086–1098.
15. Ye JC, Tak S, Han Y, Park HW. Projection reconstruction MR imaging using FOCUSS. Magn Reson Med 2007;57:764–775.
16. Pruessmann KP, Weiger M, Bornert P, Boesiger P. Advances in sensitivity encoding with arbitrary k-space trajectories. Magn Reson Med 2001;46:638–651.
17. Lustig M, Pauly JM. SPIRiT: Iterative self-consistent parallel imaging reconstruction from arbitrary k-space. Magn Reson Med 2010;64:457–471.
18. Börnert P, Aldefeld B. Principles of whole-body continuously-moving-table MRI. J Magn Reson 2008;28:1–12.
19. Han Y, Weigel M, Huff S, Ludwig U. Whole-body diffusion-weighted imaging with a continuously moving table acquisition method: preliminary results. Magn Reson Med 2011;65:1557–1563.